

# High-resolution observations of flare precursors in the low solar atmosphere

Haimin Wang<sup>1,2,3\*</sup>, Chang Liu<sup>1,2,3</sup>, Kwangsu Ahn<sup>2</sup>, Yan Xu<sup>1,2,3</sup>, Ju Jing<sup>1,2,3</sup>, Na Deng<sup>1,2,3</sup>, Nengyi Huang<sup>1,2,3</sup>, Rui Liu<sup>4,5</sup>, Kanya Kusano<sup>6</sup>, Gregory D. Fleishman<sup>3</sup>, Dale E. Gary<sup>3</sup> and Wenda Cao<sup>2,3\*</sup>

**Solar flares are generally believed to be powered by free magnetic energy stored in the corona<sup>1</sup>, but the build up of coronal energy alone may be insufficient to trigger the flare to occur<sup>2</sup>. The flare onset mechanism is a critical but poorly understood problem, insights into which could be gained from small-scale energy releases known as precursors. These precursors are observed as small pre-flare brightenings in various wavelengths<sup>3–13</sup> and also from certain small-scale magnetic configurations such as opposite-polarity fluxes<sup>14–16</sup>, where the magnetic orientation of small bipoles is opposite to that of the ambient main polarities. However, high-resolution observations of flare precursors together with the associated photospheric magnetic field dynamics are lacking. Here we study precursors of a flare using the unprecedented spatiotemporal resolution of the 1.6-m New Solar Telescope, complemented by new microwave data. Two episodes of precursor brightenings are initiated at a small-scale magnetic channel<sup>17–20</sup> (a form of opposite-polarity flux) with multiple polarity inversions and enhanced magnetic fluxes and currents, lying near the footpoints of sheared magnetic loops. Microwave spectra corroborate that these precursor emissions originate in the atmosphere. These results provide evidence of low-atmospheric small-scale energy release, possibly linked to the onset of the main flare.**

We study the 22 June 2015 M6.5 flare (SOL2015-06-22T18:23) using H $\alpha$  (line-centre and red-wing) images and photospheric vector magnetograms obtained by the recently commissioned 1.6-m New Solar Telescope (NST)<sup>21,22</sup> at Big Bear Solar Observatory (BBSO), which is stabilized by a high-order adaptive optics system (see Methods). In particular, the vector field data are taken by the Near InfraRed Imaging Spectropolarimeter (NIRIS)<sup>23</sup> at the 1.56- $\mu$ m Fe I line. These observations have the highest spatial resolution yet achieved for solar observations ( $\sim$ 70 km for H $\alpha$  and  $\sim$ 170 km for vector field) and rapid cadence (28 s for H $\alpha$  and 87 s for vector field). Also used are flare microwave spectra and time profiles from the new Expanded Owens Valley Solar Array (EOVSA; see Methods), and time profiles of hard X-ray and soft X-ray fluxes from the Reuven Ramaty High Energy Solar Spectroscopic Imager<sup>24</sup> and the Geostationary Operational Environmental Satellite-15, respectively. Ancillary data of full-disk corona images and magnetograms from the Solar Dynamics Observatory (SDO)<sup>25</sup> are additionally used.

The long-duration 22 June 2015 M6.5 flare occurred near the disk centre (8° W, 12° N) at NOAA active region 12371. Time profiles of flare emissions in different wavelengths (including hard X-ray, soft X-ray and microwave) clearly show that shortly before the flare impulsive phase starting from  $\sim$ 17:51 UT, there are two short episodes of smaller-magnitude emissions at  $\sim$ 17:24 UT and  $\sim$ 17:42 UT, which we denote as P1 and P2, respectively (see Supplementary Fig. 1). We find that these emissions can only stem from the active region of the imminent M6.5 flare, and that simultaneous H $\alpha$  brightenings are observed with NST in the flaring core region (see Supplementary Video 1). Thus they can be regarded as precursors of the M6.5 flare. Fine-structural evolution of the associated precursor brightenings in NST H $\alpha$  and the surface magnetic structure are presented in Fig. 1. Specifically, the brightening associated with the precursor episode P1 first appears as a kernel, P1a, in NST at 17:23:21 UT (also discernible in ultraviolet and extreme ultraviolet; see Supplementary Fig. 2a,d), then quickly turns into an elongated structure with another kernel, P1b (Fig. 1a and Supplementary Fig. 2b). Later, from  $\sim$ 17:38 UT, fine-scale brightening starts to be seen in the south and travels northeastward, apparently along the previously brightened regions in P1. The precursor episode P2 starts around 17:42 UT as kernel P2a (Fig. 1b), and then another, P2b, is formed in the south (Fig. 1c). All the above brightenings exhibit little propagation towards the east. From  $\sim$ 17:46 UT, one of the main flare ribbons, Fa, seems to develop from the P2a region (see Fig. 1d and Supplementary Video 1).

Regarding the precursor brightenings, we notice that P1a/P1b and P2a/P2b all lie along a narrow lane of largely positive magnetic polarity, a few arcseconds to the east of the magnetic polarity inversion line (PIL) (see Fig. 1e). The region of P1a is co-spatial with small-scale mixed polarities (discussed below) located near the footpoints of large-scale sheared arcades, which are approximately illustrated as L1 and L2 in H $\alpha$  and 193 Å (see Fig. 1f and Supplementary Fig. 2d,e). Some other brightenings are seen near the southern footpoint of L2 in the negative field region (see, for example, Supplementary Fig. 2a–d). Furthermore, precursor brightenings predominantly move along (parallel to) the PIL, in contrast to the separation motion of the main flare ribbons Fa and Fb (see Fig. 1d, Supplementary Fig. 2c, and Supplementary Video 1) away from the PIL that complies with the standard flare model<sup>26</sup>.

In Fig. 2, we present the NIRIS vector magnetic field measurement of the flare core region. The magnetic field is highly sheared

<sup>1</sup>Space Weather Research Laboratory, New Jersey Institute of Technology, University Heights, Newark, New Jersey 07102-1982, USA. <sup>2</sup>Big Bear Solar Observatory, New Jersey Institute of Technology, 40386 North Shore Lane, Big Bear City, California 92314-9672, USA. <sup>3</sup>Center for Solar-Terrestrial Research, New Jersey Institute of Technology, University Heights, Newark, New Jersey 07102-1982, USA. <sup>4</sup>CAS Key Laboratory of Geospace Environment, Department of Geophysics and Planetary Sciences, University of Science and Technology of China, Hefei 230026, China. <sup>5</sup>Collaborative Innovation Center of Astronautical Science and Technology, Hefei, China. <sup>6</sup>Institute for Space-Earth Environmental Research, Nagoya University, Furo-cho, Chikusa-ku, Nagoya, 464-8601, Japan. \*e-mail: haimin.wang@njit.edu, wenda.cao@njit.edu

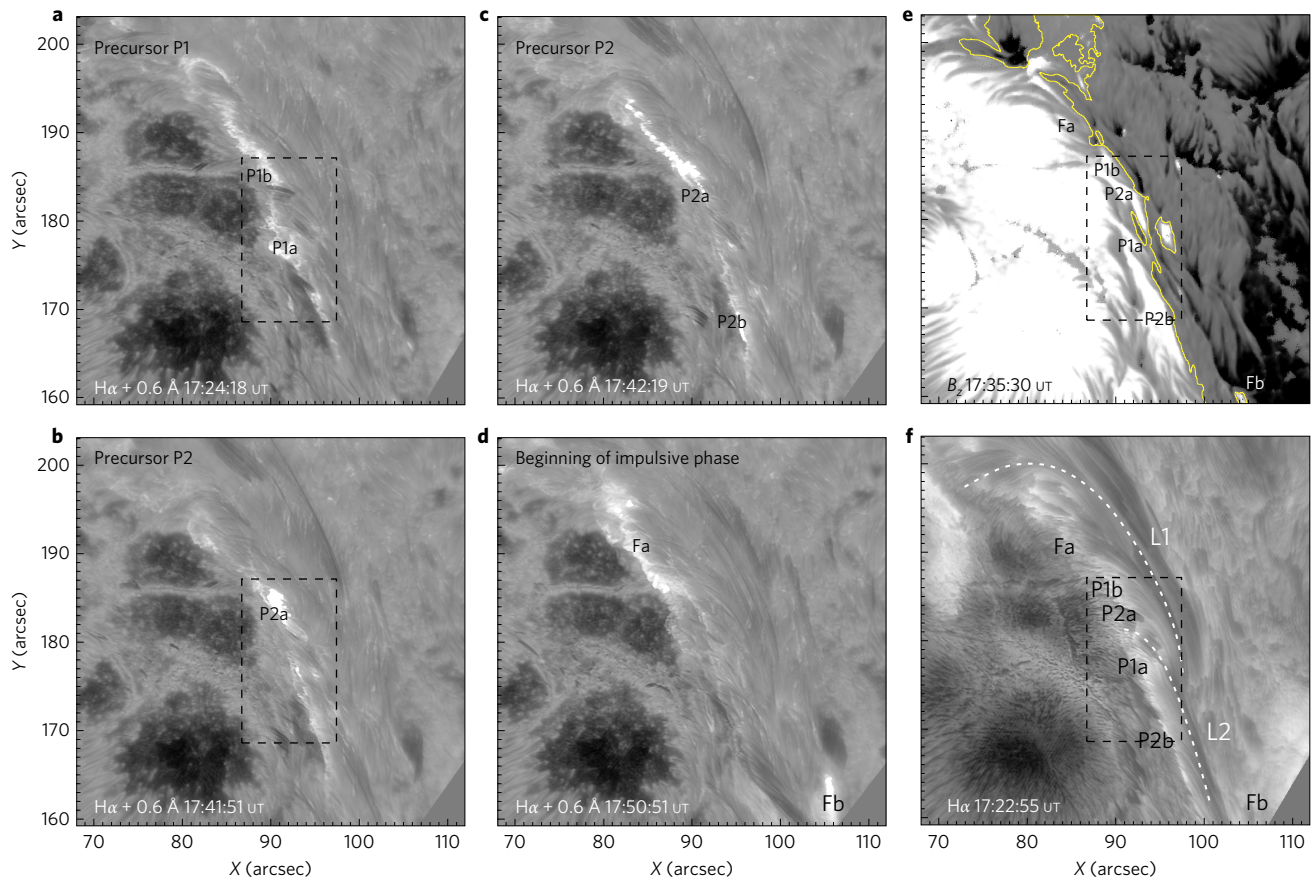


**Figure 1 | Precursor brightenings.** BBSO/NST chromospheric  $H\alpha + 0.6 \text{ \AA}$  (a–d) and  $H\alpha$  centre-line (f) images (in logarithmic greyscale) in comparison with NIRIS photospheric vertical magnetic field  $B_z$  (e; scaled between  $\pm 1,500 \text{ G}$ ), showing the core region structure of the 22 June 2015 M6.5 flare. Brightenings labelled P1a/P1b, P2a/P2b and Fa/Fb appear during the precursor episodes P1, P2, and at the beginning of the flare impulsive phase, respectively, the timings of which are indicated in Supplementary Fig. 1. The dashed box in a, b, e and f denotes the field of view of Figs 2b and 3a–c. The yellow contour in e indicates the polarity inversion line. The dashed lines in f illustrate sheared arcade loops L1 and L2 (also see Supplementary Fig. 2e). All the images were registered with respect to 22 June 2015 17:24 ut.

with respect to the PIL, especially in the precursor brightening region (Fig. 2a,b). This signifies a high degree of non-potentiality, as reflected by the concentration of magnetic shear along the PIL (Fig. 2c; see equation (1) in Methods). In the region around the initial precursor brightening P1a (enclosed by the box in Fig. 2b), we observe elongated, alternating positive and negative polarities on a fine scale of  $\sim 3,000 \text{ km}$ , constituting a miniature version of the magnetic channel structure<sup>17</sup> also recognized as the opposite-polarity type field<sup>14</sup> (see also Supplementary Video 2). Importantly, both the negative and positive fluxes within the channel exhibit an increase (by about  $-6.6 \times 10^{18}$  and  $9.3 \times 10^{18} \text{ maxwell (Mx)}$ , respectively, in about half an hour) temporally associated with the occurrence of the precursor episodes P1 and P2, and a decrease after the peak of the flare non-thermal emission (Fig. 2d). These imply that the dynamic evolution of the magnetic channel region is closely related to the triggering and subsequent evolution of the flare. It is possible to find the spatial and temporal correlation between the appearance of the precursor brightenings and the properties of the magnetic field structure and evolution because of the high spatial and temporal resolution of the NIRIS data.

We further characterize the fine-scale properties of the magnetic channel region in Fig. 3. A comparison reveals that the precursor brightenings P1a/P1b (Fig. 3a) appear in the vicinity of regions of strong vertical current density (curl of the horizontal field; calculated from equation (2) in Methods and shown in Fig. 3c), similar to what has been found previously for main flare ribbons

(for example ref. <sup>27</sup>). We also place a slit right across the magnetic channel and plot the profiles of the vertical magnetic field and current density along it (black dashed and red solid lines, respectively, in Fig. 3d). The results show 5 (11) time reversals of magnetic polarity (electric current) within  $\sim 3,000$  (6,000) km, demonstrating the complexity of this channel region at small scales. The profile of  $H\alpha + 1.0 \text{ \AA}$  along the same slit (blue dotted line in Fig. 3d) shows that the brightening has a fine structure on a scale of 500 km or less. Similar to the magnetic flux, the unsigned vertical electric current integrated over the channel region shows a clear increase (by  $\sim 5 \times 10^{11} \text{ A}$  in about half an hour) closely related to the timing of precursors P1/P2, and also a decrease after the main energy release (Fig. 2d). Such a flare-related evolutionary pattern is not found in other areas within the observed field of view. These results are suggestive that the enhancing magnetic channel structure corresponds to an emerging small current-carrying flux tube<sup>20</sup>, which might be dissipated by reconnection with ambient fields after the flare.

To extend the measurement of the magnetic field to the three-dimensional (3D) domain, we turn to the analysis of microwave observations. For reasonably uniform emission sources (such as flare precursors), the magnetic field can be derived from the total power data<sup>28</sup>. In Fig. 4a, the EOVS total-power dynamic spectrum (intensity recorded in a time-frequency diagram, averaged from the measurements of 20 dishes), with the preflare quiet Sun and active-region contribution subtracted, shows microwave flaring emissions of the two precursor episodes P1/P2 and the impulsive phase.

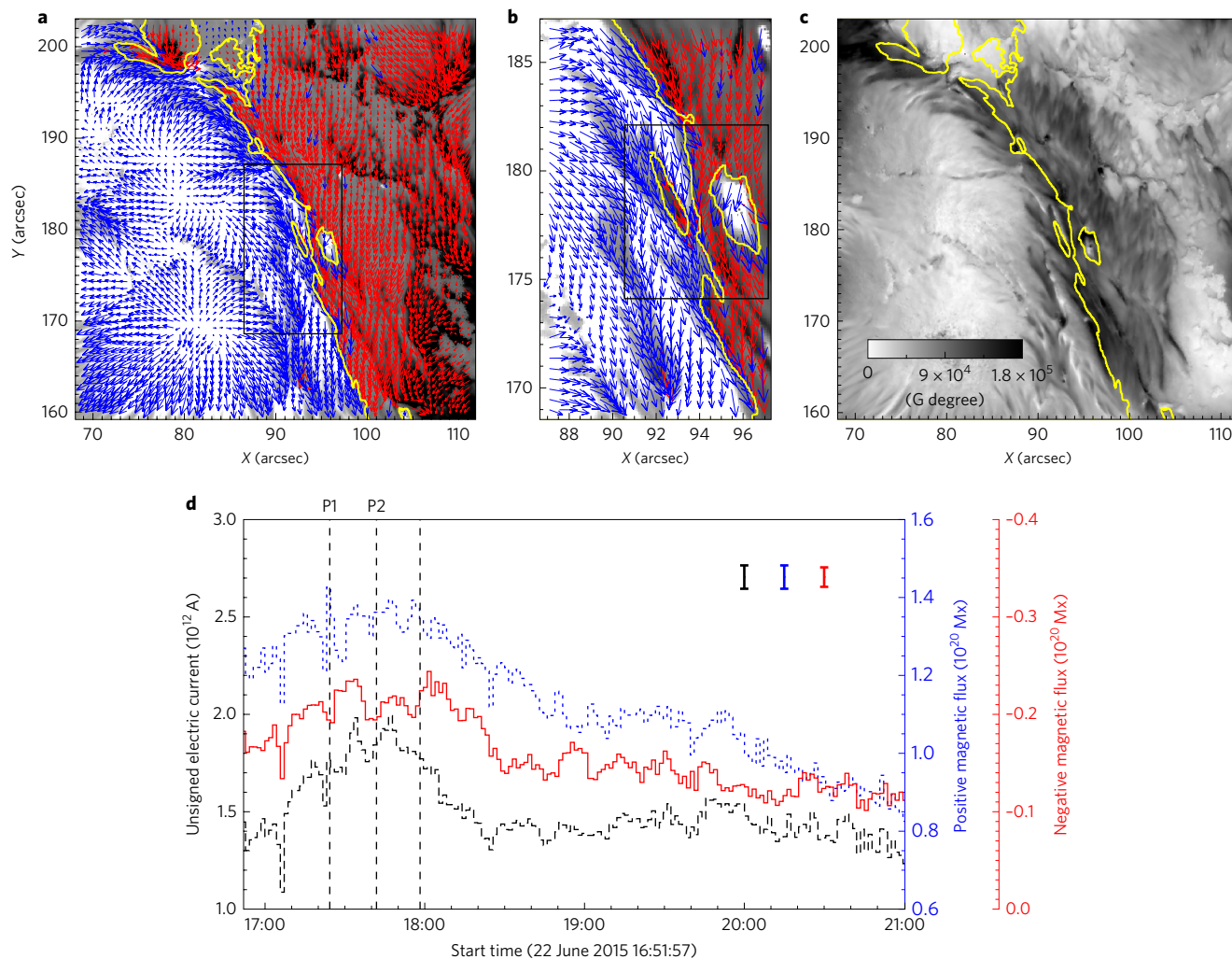


**Figure 2 | Magnetic field structure and evolution.** **a, b**, BBSO/NST NIRIS photospheric vertical magnetic field (scaled between  $\pm 1,500$  G) at 17:35:30 UT superimposed with arrows (for clarity, those in positive/negative fields are coded in blue/red) representing horizontal magnetic field vectors. The box in **a** (same as those in Fig. 1a,b,e,f) denotes the field of view of **b**, in which the magnetic channel structure can be clearly observed. **c**, Distribution of magnetic shear (see Methods). The overplotted yellow contour in **a–c** is the PIL. **d**, Temporal evolution of total positive (blue dotted line) and negative (red solid line) magnetic fluxes and the unsigned electric current (black dashed line; see Methods), calculated over the magnetic channel region enclosed by the box in **b**. The plotted representative error bars correspond to 1 s.d. calculated over the post-flare period 18:50 to 19:40 UT, demonstrating the background variation. The first two vertical dashed lines indicate the times of precursor episodes P1 and P2 at 17:24 and 17:42 UT, respectively; the third vertical dashed line denotes the peak time of the flare non-thermal emission in microwave at 17:58 UT (see Supplementary Fig. 1).

Our analyses show that the microwave spectra in the precursor periods can be modelled as quasi-thermal, gyrosynchrotron emission sources (for example Fig. 4b,c; see Methods). Their instantaneous spectral shape is determined by several physical parameters, including temperature, magnetic field and electron density<sup>29</sup>. For our purposes, we consider the temporal evolution of only the magnetic field during the precursor periods, which is derived from the spectral fittings and plotted in Fig. 4d,e. The magnetic field strengths of precursors P1 and P2 are strong ( $\geq 1,000$  G) at the beginning, then gradually decrease to a lower level (500 and 300 G, respectively). Based on the relationship between the average magnetic field strength and height above the surface as suggested by a non-linear force-free field (NLFFF) extrapolation model of this flaring region (see Methods and Supplementary Fig. 3b), this result indicates that both precursor emissions are initially located in the low atmosphere (at photospheric/chromospheric level), which corroborates the NST analysis.

Taken together, BBSO/NST  $H\alpha$  images complemented by EOVS microwave observations identify the low-atmospheric precursor

emissions in close relation to the onset of the main flare. We propose that the present event proceeds in a way consistent with the model of ref.<sup>14</sup>: an emerging small-scale flux tube, as signified by the strengthening magnetic channel<sup>20</sup> of opposite-polarity type<sup>14</sup>, interacts with and aids the reconnection of the ambient legs of large-scale sheared loops rooted in major polarities (Supplementary Fig. 2d), producing precursor brightenings. These sheared loops are also demonstrated by the NLFFF model (Supplementary Fig. 3a), in which they lie close to the surface with an apex height of  $\sim 5$  Mm. The reconnection site between the small-scale emerging flux and sheared arcades is located at the photospheric/chromospheric level; subsequently, the accelerated particles can quickly propagate and cause brightenings in other remote footpoints (for example P1c in Supplementary Fig. 2a,b,d). During the two precursor periods, the motion of  $H\alpha$  brightening kernels along the PIL may reflect the successive reconnection of different branches of the sheared arcade loops, which eventually leads to the imminent eruption of the main flare (Supplementary Fig. 2f). We made no attempt to compare our observations with other flare triggering scenarios, as

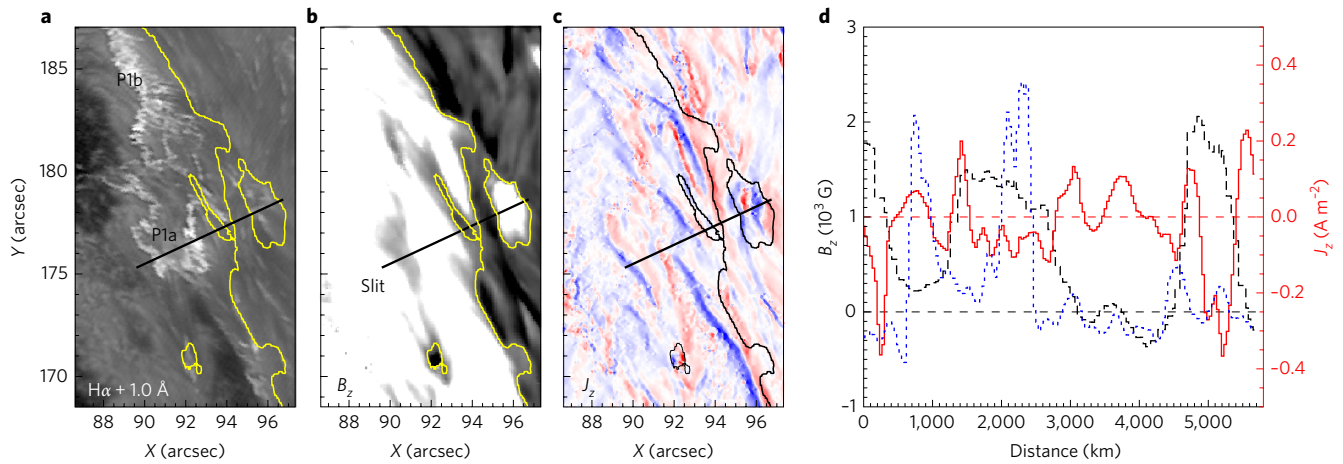


**Figure 3 | Properties of magnetic channel region.** **a**,  $H\alpha + 1.0 \text{ \AA}$  image at the time of the precursor episode P1. **b,c**, NIRIS vertical magnetic field  $B_z$  and vertical current density  $J_z$  derived from horizontal field (see Methods) at a preflare time. The field of view of **a–c** is denoted by the box in Figs 1a,b,e,f and 2a and is the same as that of Fig. 2b. The yellow (black) contour in **a** and **b (c)** is the polarity inversion line. Colour scales: **a**, linear scale in arbitrary units; **b**, range  $-500$  to  $+500$  gauss, linear scale; **c**, range  $-0.2$  (blue) to  $+0.2$  (red)  $\text{A m}^{-2}$ . **d**, Profiles of  $J_z$  (red solid line),  $B_z$  (black dashed line) and normalized  $H\alpha + 1.0 \text{ \AA}$  intensity (blue dotted line; in arbitrary units) along a slit (indicated by the thick black line in **a–c**) through the magnetic channel. The distance in the abscissa is set to zero at the southeastern end of the slit. Error bars are omitted as the uncertainties are too small compared with the axis scale.

the model of ref. <sup>14</sup> is perhaps the only one that incorporates both the small- and large-scale magnetic structures (that is, small opposite-polarity type field and overlying sheared arcades). As sheared arcade systems are often present in flaring active regions, more observations of the low solar atmosphere, especially high-resolution photospheric magnetic field measurements with good temporal coverage, are desirable. This would allow the problem of the flare onset mechanism to be better understood, as is needed for improving forecasts of space weather.

## Methods

**Optical wavelength observations and reduction.** The NST is a 1.6-m off-axis telescope at BBSO operated by the New Jersey Institute of Technology. Currently, it produces the highest-spatial-resolution (for example, 70 km when observing around 6,000  $\text{\AA}$ ), diffraction-limited observations of the Sun, aided by a 308-element adaptive optics system and speckle-masking image reconstruction. During the period of  $\sim 16:50\text{--}23:00$  UT on 22 June 2015, NST observed the M6.6 flare at NOAA AR 12371. The data taken include spectroscopic observations in  $H\alpha$  line centre and  $\pm 0.6$  and  $\pm 1.0 \text{ \AA}$  (with a bandpass of 0.07  $\text{\AA}$ ), and also images in the TiO band (a proxy for the continuum photosphere around 7,057  $\text{\AA}$ ). The images have a spatial resolution of  $\sim 70\text{--}80$  km and a cadence ranging from 15 to 28 s.

Notably, this study makes the first scientific use of data from NIRIS, which measured the photospheric magnetic field during this observation run. This is also NIRIS's first coverage of a flare observed with NST. NIRIS uses dual Fabry–Pérot etalons that provide a 60,000 km  $\times$  60,000 km field of view and a great throughput of over 90%. NIRIS achieves a spatial resolution of  $\sim 170$  km at the 1.56- $\mu\text{m}$  Fe I line (with a bandpass of 0.1  $\text{\AA}$ ). The cadence of NIRIS data (full set of vector magnetograms) for this 22 June 2015 observation run is 87 s. The 1.56- $\mu\text{m}$  line offers a high Landé  $g$ -factor of 3, which can help to increase the signal strength of magnetograms. Although this line has a lower diffraction limit than some visible lines, it produces much more stable images under atmospheric turbulence.

For the NIRIS observations, first the dual-beam optical design images two simultaneous polarization states onto a 2,024  $\times$  2,048 HgCdTe closed-cycle infrared array that undergoes thermo-electric cooling. A combination of a linear polarizer and a quarter-wave plate is used in the telescope structure to create pure polarization states, after which the responses of the following optical elements through the detector are measured. This approach is able to eliminate the crosstalk among the Stokes Q, U and V parameters.

Second, the NIRIS data undergoes Stokes inversion using the Milne–Eddington technique, through which several key physical parameters (including total magnetic field, azimuth angle, inclination and Doppler shift) can be extracted. For successful fittings with Milne–Eddington-simulated profiles, initial parameters are pre-calculated to be close to the observed Stokes profiles<sup>30</sup>. The accuracy of the resulted vector field data is 10 G for the line-of-sight component and 100 G for the transverse component.

For this 22 June 2015 observation, we validate the NIRIS data by checking against those obtained from two spaceborne instruments, the spectropolarimeter (SP) of Hinode's 0.5-m Solar Optical Telescope<sup>31</sup> and SDO's Helioseismic and Magnetic Imager (HMI)<sup>32</sup>. Hinode/SP and SDO/HMI have spatial resolutions of about 230 and 725 km, and temporal cadences of a few hours and 12 minutes, respectively. In Supplementary Fig. 4, we compare line-of-sight field, transverse field and azimuthal angle from the three instruments measured around 22 June 2015 22:35 UT. It can be clearly seen that the magnetic structures observed by NIRIS, Hinode/SP and SDO/HMI are highly similar, but more details are present in NIRIS data, owing to its higher spatial resolution. A cross-correlation analysis reveals that data acquired by NIRIS match well with those taken by Hinode/SP and SDO/HMI, with correlation coefficients of 0.97, 0.9 and 0.8 for the line-of-sight field, transverse field and azimuthal angle measurements, respectively. This demonstrates the superiority of NIRIS observations in making high-spatiotemporal-resolution studies of photospheric magnetic field evolution.

Third, to explore the magnetic field structure properly, we further process the NIRIS vector magnetograms resulting from inversion, to resolve the 180° azimuthal ambiguity using the ME0 code<sup>33</sup>, which is based on the 'minimum energy' ambiguity resolution method<sup>34,35</sup>, and to remove the projection effects by transforming the observed vector fields (line-of-sight and transverse) to those in heliographic coordinates (vertical  $B_z$  and horizontal  $B_x$  and  $B_y$  fields) using the equations of ref.<sup>36</sup>. To characterize the non-potentiality of the active region, we calculate magnetic shear  $S$ , defined as the product of field strength and shear angle<sup>37,38</sup>:

$$S = |B|\theta \quad (1)$$

where  $\theta = \cos^{-1}[(\mathbf{B} \cdot \mathbf{B}_p)/(B B_p)]$ , and the subscript  $p$  represents the potential field (here computed using the Green's function method<sup>39</sup>). We also derive the vertical current density  $J_z$ :

$$J_z = \frac{1}{\mu_0} (\nabla \times \mathbf{B})_z = \frac{1}{\mu_0} \left( \frac{\partial B_y}{\partial x} - \frac{\partial B_x}{\partial y} \right) \quad (2)$$

where  $\mu_0$  is the permeability of the vacuum.

**Full-disk observations for context.** We complement high-resolution NST data with full-disk SDO observations for a better understanding of the overall picture of the flare. Images shown in Supplementary Fig. 2 include those from SDO's Atmospheric Imaging Assembly<sup>40</sup> 1,700- $\text{\AA}$  (temperature minimum region and photosphere), 193- $\text{\AA}$  (corona and hot flare plasma) and 94- $\text{\AA}$  (hot flare plasma) passbands, and SDO's HMI.

**Microwave observation and analysis.** This study also makes the first scientific use of the EOVS data. EOVS is a newly upgraded, solar-dedicated radio array consisting of 13 antennas of 2.1-m diameter, which are equipped with receivers designed to cover the frequency range 1–18 GHz. Two large (27-m diameter) dishes are being outfitted with He-cooled receivers for use in calibration of the small dishes<sup>41</sup>. EOVS has just started scientific operation.

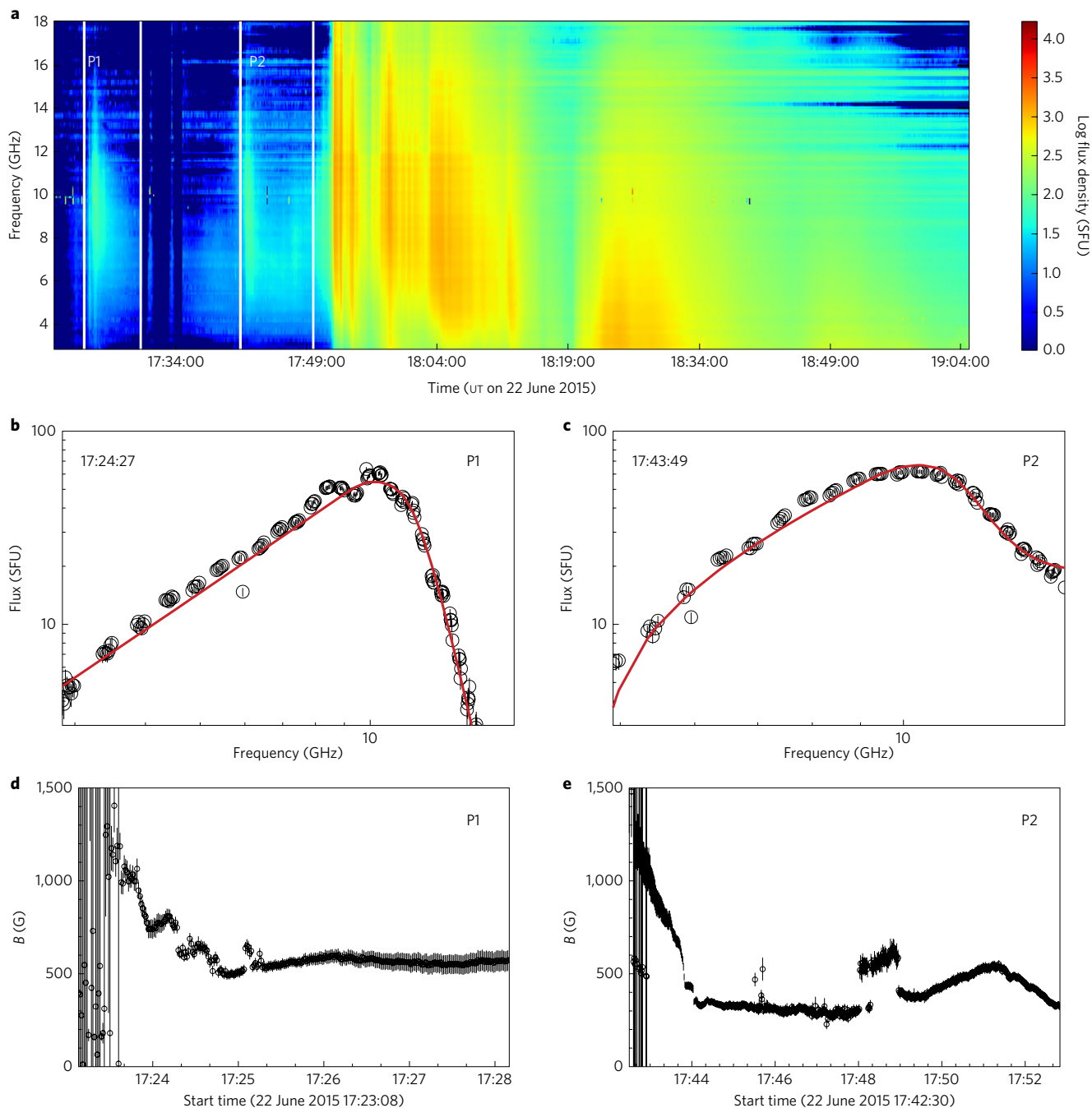


**Figure 4 | Microwave emission.** **a**, EOVSA total power dynamic spectra (with the preflare quiet Sun and AR contribution subtracted) of microwave emission, covering two precursor episodes P1 and P2 and the impulsive phase of the flare. The four white vertical stripes are data gaps. **b,c**, Sample spectral fittings at P1 and P2 using a gyrosynchrotron source function (see Methods). **d,e**, Evolution of the derived magnetic field strength in the two precursor periods. The error bars represent 1 s.d. statistical errors returned by the spectral fit. SFU, solar flux unit.

For the event under study, the EOVSA microwave observation covers both the precursors and the main flare. Although the microwave spectrum is broadband during the main flare (which is a result of source non-uniformity in space), the preflare phase demonstrates reasonably narrow spectra consistent with a quasi-uniform source. This kind of source can be conclusively forward-fitted using the gyrosynchrotron source function to recover the physical parameters responsible for the observed spectral shape<sup>28</sup>. Inspection of the detailed spectral shape at the preflare phase reveals that the spectra are almost thermal, which greatly simplifies the fitting and enhances the reliability of the fit results<sup>12</sup>. To define the gyrosynchrotron source function quantitatively, we use the fast gyrosynchrotron codes developed in ref.<sup>42</sup> and apply the optimization scheme as described in ref.<sup>43</sup>. The fit returns evolution of the plasma density, temperature and magnetic field strength (as shown in Fig. 4d,e). In this analysis, we focus on the evolution of magnetic field at the instantaneous

location of the radio burst, which recovers a significant elevation of the radio source with time and thus allows us to extend the analysis to the 3D domain. The use of a magnetic field extrapolation model (see below) maps the coronal magnetic field probed from the microwave data to the actual heights above the active region.

**Coronal magnetic field extrapolation.** To disclose the magnetic structure above the flaring active region, we use the NLFFF extrapolation technique to construct a 3D magnetic field. As NIRIS data have a limited field of view, we base the magnetic field modelling on the lower-resolution SDO/HMI vector data. A preprocessing procedure<sup>44</sup> is first performed to minimize the net force and torque in the observed photospheric field. A ‘weighted optimization’ method<sup>45,46</sup> is then applied to derive the NLFFF, from which magnetic field lines are computed. Physical properties of field lines, such as the magnetic twist, can be further deduced<sup>47</sup>.

**Data availability.** The data that support the plots within this paper and other findings of this study are available from the corresponding authors upon reasonable request.

Received 11 October 2016; accepted 22 February 2017;  
published 27 March 2017

## References

- Priest, E. R. & Forbes, T. G. The magnetic nature of solar flares. *Astron. Astrophys. Rev.* **10**, 313–377 (2002).
- Benz, A. O. Flare observations. *Living Rev. Sol. Phys.* **5**, 1 (2008).
- Bumba, V. & Křivský, L. Chromospheric pre-flares. *Bull. Astron. Inst. Czech J.* **10**, 221–223 (1959).
- Martin, S. F. Preflare conditions, changes and events. *Sol. Phys.* **68**, 217–236 (1980).
- van Hoven, G. & Hurford, G. J. Solar flare precursors. *Adv. Space Res.* **6**, 83–91 (1986).
- Kai, K., Nakajima, H. & Kosugi, T. Radio observations of small activity prior to main energy release in solar flares. *Publ. Astron. Soc. Jpn* **35**, 285–297 (1983).
- Warren, H. P. & Marshall, A. D. Ultraviolet flare ribbon brightenings and the onset of hard X-ray emission. *Astrophys. J. Lett.* **560**, L87–L90 (2001).
- Asai, A. *et al.* Preflare nonthermal emission observed in microwaves and hard X-rays. *Publ. Astron. Soc. Jpn* **58**, L1–L5 (2006).
- Chifor, C., Tripathi, D., Mason, H. E. & Dennis, B. R. X-ray precursors to flares and filament eruptions. *Astron. Astrophys.* **472**, 967–979 (2007).
- Battaglia, M., Fletcher, L. & Benz, A. O. Observations of conduction driven evaporation in the early rise phase of solar flares. *Astron. Astrophys.* **498**, 891–900 (2009).
- Altynsev, A. A., Fleishman, G. D., Lesovoi, S. V. & Meshalkina, N. S. Thermal to nonthermal energy partition at the early rise phase of solar flares. *Astrophys. J.* **758**, 138 (2012).
- Fleishman, G. D., Nita, G. M. & Gary, D. E. Energy partitions and evolution in a purely thermal solar flare. *Astrophys. J.* **802**, 122 (2015).
- Zhang, Y. *et al.* Solar radio bursts with spectral fine structures in preflares. *Astrophys. J.* **799**, 30 (2015).
- Kusano, K. *et al.* Magnetic field structures triggering solar flares and coronal mass ejections. *Astrophys. J.* **760**, 31 (2012).
- Toriumi, S. *et al.* The magnetic systems triggering the M6.6 class solar flare in NOAA active region 11158. *Astrophys. J.* **773**, 128 (2013).
- Bamba, Y., Kusano, K., Yamamoto, T. T. & Okamoto, T. J. Study on the triggering process of solar flares based on Hinode/SOT observations. *Astrophys. J.* **778**, 48 (2013).
- Zirin, H. & Wang, H. Narrow lanes of transverse magnetic field in sunspots. *Nature* **363**, 426–428 (1993).
- Kubo, M. *et al.* Hinode observations of a vector magnetic field change associated with a flare on 2006 December 13. *Publ. Astron. Soc. Jpn* **59**, S779–S784 (2007).
- Wang, H., Jing, J., Tan, C., Wiegelmann, T. & Kubo, M. Study of magnetic channel structure in active region 10930. *Astrophys. J.* **687**, 658–667 (2008).
- Lim, E.-K., Chae, J., Jing, J., Wang, H. & Wiegelmann, T. The formation of a magnetic channel by the emergence of current-carrying magnetic fields. *Astrophys. J.* **719**, 403–414 (2010).
- Goode, P. R., Coulter, R., Gorceix, N., Yurchyshyn, V. & Cao, W. The NST: first results and some lessons for ATST and EST. *Astron. Nachr.* **331**, 620–623 (2010).
- Cao, W. *et al.* Scientific instrumentation for the 1.6 m New Solar Telescope in Big Bear. *Astron. Nachr.* **331**, 636–639 (2010).
- Cao, W. *et al.* NIRIS: the second generation near-infrared imaging spectropolarimeter for the 1.6 meter New Solar Telescope. *Astron. Soc. Pacif. Conf. Series* **463**, 291–299 (2012).
- Lin, R. P. *et al.* The Reuven Ramaty High-Energy Solar Spectroscopic Imager (RHESSI). *Sol. Phys.* **210**, 3–32 (2002).
- Pesnell, W. D., Thompson, B. J. & Chamberlin, P. C. The Solar Dynamics Observatory (SDO). *Sol. Phys.* **275**, 3–15 (2012).
- Kopp, R. A. & Pneuman, G. W. Magnetic reconnection in the corona and the loop prominence phenomenon. *Sol. Phys.* **50**, 85–98 (1976).
- Janvier, M. *et al.* Electric currents in flare ribbons: observations and three-dimensional standard model. *Astrophys. J.* **788**, 60 (2014).
- Fleishman, G. D., Nita, G. M., Kontar, E. P. & Gary, D. E. Narrowband gyrosynchrotron bursts: probing electron acceleration in solar flares. *Astrophys. J.* **826**, 38 (2016).
- Stahli, M., Gary, D. E. & Hurford, G. J. High-resolution microwave spectra of solar bursts. *Sol. Phys.* **120**, 351–368 (1989).
- Ahn, K., Cao, W., Shumko, S. & Chae, J. Data processing of the magnetograms for the Near InfraRed Imaging Spectropolarimeter at Big Bear Solar Observatory. *Am. Astron. Soc. Sol. Phys. Div. Meeting* **47**, 2.07 (2016); <https://ui.adsabs.harvard.edu/#abs/2016SPD...47.0207A/abstract>
- Tsuneta, S. *et al.* The Solar Optical Telescope for the Hinode mission: an overview. *Sol. Phys.* **249**, 167–196 (2008).
- Shou, J. *et al.* Design and ground calibration of the Helioseismic and Magnetic Imager (HMI) instrument on the Solar Dynamics Observatory (SDO). *Sol. Phys.* **275**, 229–259 (2012).
- Leka, K. D., Barnes, G. & Crouch, A. An automated ambiguity-resolution code for Hinode/SP vector magnetic field data. *Astron. Soc. Pacif. Conf. Series* **415**, 365–368 (2009).
- Metcalf, T. R. Resolving the 180-degree ambiguity in vector magnetic field measurements: the ‘minimum’ energy solution. *Sol. Phys.* **155**, 235–242 (1994).
- Metcalf, T. R. *et al.* An overview of existing algorithms for resolving the 180° ambiguity in vector magnetic fields: quantitative tests with synthetic data. *Sol. Phys.* **237**, 267–296 (2006).
- Gary, G. A. & Hagyard, M. J. Transformation of vector magnetograms and the problems associated with the effects of perspective and the azimuthal ambiguity. *Sol. Phys.* **126**, 21–36 (1990).
- Wang, H., Ewell, M. W. Jr, Zirin, H. & Ai, G. Vector magnetic field changes associated with X-class flares. *Astrophys. J.* **424**, 436–443 (1994).
- Wang, H. *et al.* The relationship between magnetic gradient and magnetic shear in five super active regions producing great flares. *Chinese J. Astron. Astr.* **6**, 477–488 (2006).
- Metcalf, T. R. *et al.* Nonlinear force-free modeling of coronal magnetic fields. II. Modeling a filament arcade and simulated chromospheric and photospheric vector fields. *Sol. Phys.* **247**, 269–299 (2008).
- Lemen, J. R. *et al.* The Atmospheric Imaging Assembly (AIA) on the Solar Dynamics Observatory (SDO). *Sol. Phys.* **275**, 17–40 (2012).
- Gary, D. E. Early observations with the expanded Owens Valley Solar Array. *Am. Astron. Soc. Sol. Phys. Div. Meeting* **47**, 301.01 (2016); <https://ui.adsabs.harvard.edu/#abs/2016SPD...4730101G/abstract>
- Fleishman, G. D. & Kuznetsov, A. A. Fast gyrosynchrotron codes. *Astrophys. J.* **721**, 1127–1141 (2010).
- Fleishman, G. D., Nita, G. M. & Gary, D. E. Dynamic magnetography of solar flaring loops. *Astrophys. J. Lett.* **698**, L183–L187 (2009).
- Wiegelmann, T., Inhester, B. & Sakurai, T. Preprocessing of vector magnetograph data for a nonlinear force-free magnetic field reconstruction. *Sol. Phys.* **233**, 215–232 (2006).
- Wheatland, M. S., Sturrock, P. A. & Roumeliotis, G. An optimization approach to reconstructing force-free fields. *Astrophys. J.* **540**, 1150–1155 (2000).
- Wiegelmann, T. Optimization code with weighting function for the reconstruction of coronal magnetic fields. *Sol. Phys.* **219**, 87–108 (2004).
- Liu, R. *et al.* Structure, stability, and evolution of magnetic flux ropes from the perspective of magnetic twist. *Astrophys. J.* **818**, 148 (2016).

## Acknowledgements

We thank the BBSO, EOVS, SDO, RHESSI, GOES and Hinode teams for obtaining the data. This work was supported by NASA under grants NNX13AF76G, NNX13AG13G, NNX14AC12G, NNX14AC87G, NNX16AL67G and NNX16AF72G, and by the NSF under grants AGS 1250374, 1262772, 1250818, 1348513, 1408703 and 1539791. R.L. acknowledges support from the Thousand Young Talents Program of China and NSFC 41474151. K.K. acknowledges support from MEXT/JSPS KAKENHI 15H05814. The BBSO operation is supported by NJIT, US NSF AGS 1250818 and NASA NNX13AG14G grants, and partly supported by the Korea Astronomy and Space Science Institute and Seoul National University and by the Chinese Academy of Science’s strategic priority research programme, Grant No. XDB09000000.

## Author contributions

H.W. initiated the idea and carried out the data processing, analysis, interpretation and manuscript writing. C.L. contributed to the azimuth disambiguation of NIRIS data, data analysis and interpretation, and manuscript revision. K.A. developed tools for NIRIS data calibration, polarization inversion, and processed the NIRIS data. Y.X. was the Principal Investigator for this BBSO/NST observation run and contributed to the data processing. J.J. and N.D. contributed to the data analysis. N.H. contributed to this NST observation run. R.L. contributed to the NLFFF modelling and result interpretation. K.K. contributed to the interpretation of observations. G.D.F. and D.E.G. carried out the microwave data analysis and modelling. W.C. developed instruments at BBSO. All authors discussed the results and commented on the manuscript.

## Additional information

Supplementary information is available for this paper.

Reprints and permissions information is available at [www.nature.com/reprints](http://www.nature.com/reprints).

Correspondence and requests for materials should be addressed to H.W. and W.C.

How to cite this article: Wang, H. *et al.* High-resolution observations of flare precursors in the low solar atmosphere. *Nat. Astron.* **1**, 0085 (2017).

Publisher’s note: Springer Nature remains neutral with regard to jurisdictional claims in published maps and institutional affiliations.

## Competing interests

The authors declare no competing financial interests.